Characteristics of optical emission during laser-induced damage events of fused silica

Chao Shen (沈 超)[1,2,*], Nanjing Zhao (赵南京)[1,2], Jaka Pribošek[3], Mingjun Ma (马明俊)[1,2], Li Fang (方 丽)[1,2], Xingjiu Huang (黄行九)[4], and Yujun Zhang (张玉钧)[5,]**

[1]*Key Laboratory of Environmental Optics & Technology, Anhui Institute of Optics and Fine Mechanics, Chinese Academy of Sciences, Hefei 230031, China*

[2]*Key Laboratory of Optical Monitoring Technology for Environment, Hefei 230031, China*

[3]*Carinthian Tech Research, 9524 Villach, Austria*

[4]*Institute of Intelligent Machines, Chinese Academy of Sciences, Hefei 230031, China*

[5]*State Key Laboratory of Pulsed Power Laser Technology, National University of Defense Technology, Hefei 230037, China*

**Corresponding author: cshen@aiofm.ac.cn; **corresponding author: yjzhang@aiofm.ac.cn*

Received August 8, 2019; accepted August 30, 2019; posted online December 2, 2019

Spontaneous optical emission properties of laser-produced plasma during laser damage events at input and exit surfaces of fused silica were retrieved and compared. We show that plasma at the input surface is much larger in size and exhibits significantly higher electron number density and excitation temperature, even when smaller laser energy was used. This effect was attributed to the stronger laser–plasma coupling at the input surface. In addition, a strong continuum background containing three peaks at 1.3 eV, 1.9 eV, and 2.2 eV was observed at the exit surface, and possible origins for this effect are also discussed.

OCIS codes: 300.6365, 140.3330, 140.3440.
doi: 10.3788/COL201917.123002.

During many pulsed laser-induced damage (LID) events, the incident laser intensity can be high enough to transfer adequate energy to the target to produce a vaporized layer and cause atomization and ionization processes in vapor. The ionized vapor can absorb incident laser energy to further increase its temperature and subsequently induce the breakdown of vapor and the formation of plasma[1,2]. This laser-produced plasma (LPP) has a strong and spontaneous broadband optical emission and exhibits as a bright fireball[3–6]. Due to its intrinsic characteristics of high pressure, temperature, and electron number density, LPP usually produces additional effects on LID sites, such as causing a burning scar around the LID site on optical coatings[7,8] and assisting the formation of periodical structures on the target surface by facilitating the interference between incident laser beams and beams reflected by the plasma[9,10]. The role of LPP is particularly important in LID of transparent optical components because the laser can penetrate the component and generate plasma plumes at either the input or exit surface[11]. For input surface damage, LPP can directly interact with the incident laser pulse, and the laser energy is mainly deposited in LPP. By contrast, the laser pulse first interacts with the target bulk during exit surface damage, and the laser energy is mainly deposited in bulk material. Although the LPP is one of the most obvious manifestations of this disparity between input and exit surface damage, limited works have been reported focusing on LPPs formed on different surfaces. Salleo *et al.*[12] have compared the propagation of shock waves formed by the expansion of air part LPPs in input and exit surface damage events of fused silica induced by a 35 ps infrared pulse. It was shown that the input surface shock wave is stronger, and the deduced driving energy is more than twice that of the exit surface one. Liu *et al.*[13] have observed similar results in the same target under the irradiation of a 6.8 ns ultraviolet pulse. They attributed this asymmetry to different expansion pressures of LPPs. These results, however, are only based on absorption or refraction techniques such as shadowgraphy and the laser-deflection method and do not involve emission properties of LPP. Zeng *et al.*[14–17] investigated the emission spectra of input surface plasma produced by 266 nm nanosecond pulses on fused silica. Using the Stark broadening effect of a 288.16 nm Si I line and the line-to-continuum ratio method, they found that the electron number density and temperature of plasma could reach 10^{18} cm^{-3} and 10^4 K. However, they only performed damage on the input surface, and they mainly focused on the comparison between plasma produced on the flat surface and the cavity structure. Raman *et al.*[18] have performed the pioneer work focusing on the emission spectra of the exit surface LPP induced by 355 nm nanosecond pulses. They recorded a continuum background in the visible range superimposed with two peaks from nitrogen and Si; however, in their work, no further details concerning the plasma parameters were discussed. Recently, Harris *et al.*[19] presented a more detailed discussion about the exit surface plasma, and they deduced an electron number density of around 10^{17} cm^{-3} and plasma temperature of higher than 10^4 K. However, plasmas investigated in this work were produced on the surface attached with steel microspheres, and thus, obvious plasma confinement

effects should be anticipated between the sample and microsphere surface. This is different from the usual exit surface plasmas, which are produced on the flat surface. Overall, although several works have discussed the surface damage plasma, direct comparison of plasma emission properties between input and exit surface damages is still not reported.

In this Letter, we report a comparison of optical emission properties between LPPs on different surfaces of fused silica under the irradiation of an 8 ns infrared pulse. The spontaneous emission image and spectra of LPP on both surfaces are recorded, and spectroscopic parameters such as electron density and temperature are retrieved using Stark broadening and the Boltzmann plot method. The goal of this work is to present a preliminary comparison of optical emission properties on different surfaces during LID of fused silica.

The schematic of the experimental setup is shown in Fig. 1. A 1064 nm Q-switched Nd-doped yttrium aluminum garnet (Nd:YAG) nanosecond laser (Quantel, Ultra-100) with a width of 8 ns was used to produce LID on fused silica surfaces. The maximum energy output from this laser was ~100 mJ and could be attenuated to less than 1 mJ using the combination of a half-wavelength waveplate and a Glan–Taylor prism. The laser energy before focusing was monitored using an energy meter (Ophir). The laser beam was focused by a double-convex lens with a focal length of 50.8 mm (N.A. = 0.08), and the beam was focused as an ellipse in the focal position with a beam semidiameter ($1/e^2$) of 24.5 μm and 35 μm in the horizontal and vertical directions, respectively. We would like to stress that the choice of N.A. of the focusing beam is a trade-off between tight focus to avoid damage or plasma ignition at the other surface and the amount of spherical aberration introduced by the dielectric plate. Zemax ray tracing simulation was performed to find that beam size is dominated by a spherical aberration of the focusing lens (max optical path difference $< \lambda/3$) with negligible aberrations induced from the dielectric plate. According to our simulation, a focal length of 50.8 mm is a good compromise to make sure that the beam spots on both surfaces are equal while the Rayleigh distance is small enough (~2.5 mm) not to damage other surfaces.

A home-made microscope equipped with an objective lens with a focal length of 40 mm (Mitutoyo, N.A. = 0.14) and a digital color complementary metal–oxide–semiconductor (CMOS) camera (Thorlabs) was used to capture the plasma image. The microscope was focused on the lateral side of the plasma to facilitate the record of the plasma length. A 50:50 beam splitter placed between the objective and tube lens was used to split the plasma emission spectra into the camera and a fiber-based spectrometer (Avantes) evenly. The focal length of the tube lens for the camera is 200 mm, corresponding to a magnification of five times and a resolution of better than 2.2 μm/pixel. The focal length of the tube lens for the fiber collector is 30 mm, giving a magnification of 0.75 times. With a fiber diameter of 1.75 mm, a maximum plasma volume of ~2.3 mm could be observed. The spectrometer wavelength range is 500–1030 nm with a 0.1 nm resolution, and the time delay and gate width were 1.28 μs and 1.05 ms, respectively. The exposure time of camera was 66 ms. The camera and spectrometer worked in the trigger mode and were synchronized with the output signal of the laser. A three-dimensional mechanical stage was used to place the fused silica windows so that they could be translated after each laser pulse to avoid repetitive damages. To place the sample surface in the focal position precisely, the position of air plasma was first recorded using the five times microscope. Then, for both the exit and input surface damages, the designated surface was placed along the middle of the plasma (indicated as the red dashed line in the inset of Fig. 1). For exit surface damage, the sample position was further adjusted to compensate for defocus induced by the refraction at the input surface of the sample. This is experimentally achieved by finding the position with the most severe damage sites and the highest echo level of plasma.

Figure 2 illustrates typical shapes of plasma plumes in air during surface damage events at the fused silica

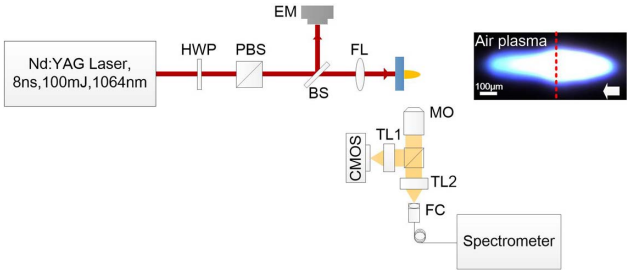

Fig. 1. Schematic of experimental setup. The inset is the image of air plasma. The red dashed line is the position of the sample surface, and the white arrow indicates the direction of the laser pulse. The arrangements of the camera and spectrometer are set as an example of the exit surface damage. HWP, half-wavelength plate; PBS, polarized beam splitter; BS, beam splitter; EM, energy meter; FL, focus lens; FC, fiber collector; MO, microscope objective; TL, tube lens.

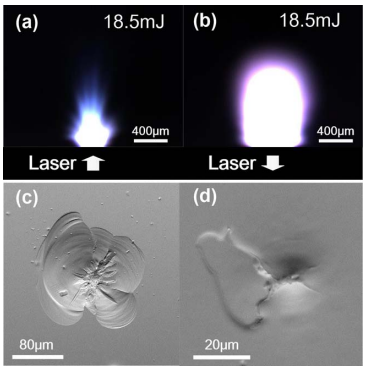

Fig. 2. Typical images of LPP on (a) the exit surface and (b) the input surface. Scanning electron microscope (SEM) morphologies of damage sites on (c) the exit surface and (d) the input surface.

input and exit surfaces, respectively. For both surfaces, plasmas are shown as semielliptical in shape with a bright plasma core and a less bright edge, which are the representative shapes of air side plasmas formed in laser-ablation-related applications[20]. Comparing the shapes between input and exit surface plasma, we see that the core boundary is much more irregular at the exit surface. As the shape of the plasma core seldom changes from pulse to pulse, the irregularity is not likely to be formed by turbulences. Several works[21,22] have reported similar irregular plume shapes, and ejection and ionization of massive materials was attributed to the irregularity[21]. Therefore, a less disturbed plasma core can be anticipated in the input surface because the quantity of ejected bulk material is much lower. This is proved by the inspection of the morphology of the damage sites on both surfaces, as shown in Figs. 2(c) and 2(d). A much more severe damaged site can be observed on the exit surface, indicating the occurrence of a more violent ejection process[23,24]. For the exit surface damage site, it contains a molten core, which is comparable to the beam size, and a much larger stripped periphery. The core is most probably formed during the laser pulse, as the temperature during this phase is much higher. The shape of the core is determined by the propagation of the high-temperature-induced absorption front[25], and the core depth is determined by the quantity of ejected superheated droplets[26]. The periphery is formed due to the release of stress formed in the early phase and can be identified in the ejecta as large irregular flakes. For the front surface damage site, the main mechanism is laser spallation induced by the thermal stress in the material and the recoil pressure induced by the expanding plasma. Therefore, the input surface damage is less severe and mainly manifested as mechanical damage with plastic deformation [Fig. 2(d)]. The color of the plasma edge is mainly contributed by emissions of excited air and sample particles. Emissions of excited nitrogen, oxygen molecules (400–450 nm)[27], hydrogen atoms (~656 nm), and silicon ions (~635 nm) contribute to the blue and red components, respectively. The purple color is due to the mixture of blue and red on the digital camera's red–green–blue (RGB) filter (Bayer filter). The lack of a red component in the exit surface LPP indicates a lower degree of ionization, which will be discussed in detail below.

With the increase of laser energy, plasma sizes grow but still maintain the semielliptical shape during the energy range used in this experiment. Moreover, exit surface LPPs exhibit a smaller size compared to input surface LPPs, even with much higher laser energy. This can be seen more clearly in Fig. 3(a), which illustrates the quantitative growth of the radii of plasma on both surfaces in the axial direction. The radius–energy relationship can be well fitted by the power law and fitted coefficients of input surface plasmas that are larger than exit surface ones, indicating that the input surface plasma is more sensitive to the variation of laser energy. This can be well understood because the laser–plasma interaction is much stronger on

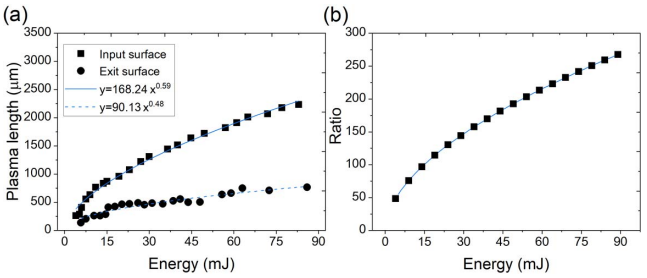

Fig. 3. (a) Evolution of plasma size with laser energy on the input and exit surfaces, and (b) the ratio between the driving energy on both surfaces deduced by Sedov–Taylor scaling.

the input surface. According to Sedov–Taylor scaling[28], the analytical relation between plasma radius R (indicated by the axial radius and estimated using a circle with the same area) and driving energy E is

$$R = c\left(\frac{E}{\rho}\right)^{0.2} t^{0.4}, \tag{1}$$

where c is a dimensionless constant, ρ is the mass density of unperturbed air, and t is the plasma expansion time. As the observation time of input and exit surface plasmas is fixed during the experiment, it is reasonable to assume that t is the same for each data in Fig. 3(a). Therefore, the ratio between the driving energy of plasma on the input and exit surfaces can be expressed as[26]

$$\frac{E_{\text{in}}}{E_{\text{ex}}} = \left(\frac{R_{\text{in}}}{R_{\text{ex}}}\right)^5, \tag{2}$$

where $E_{\text{in/ex}}$ and $R_{\text{in/ex}}$ are the driving energy and radius of input/exit surface plasma, respectively. This ratio shown in Fig. 3(b) is calculated using the fitted power law given in Fig. 3(a). The ratio increases with incident laser energy and can reach more than 100 at energies higher than 15 mJ. These results are remarkably higher than the results reported by Ref. [12], where the largest ratio is about 2.6. We attribute this discrepancy to the different laser pulse width used in each experiment. The pulse width in this work (8 ns) is much longer than the one used in Ref. [12] (35 ps). Therefore, plasmas produced in this work have the opportunity to absorb the laser energy at the trailing part of the pulse by the photoionization and inverse bremsstrahlung mechanisms[29], inducing a more efficient laser–plasma coupling process. Moreover, the peak laser power used in this work (1–11 MW) is mostly higher than the critical power of stimulated Brillouin scattering (0.22 MW) and Kerr-induced self-focusing (4.3 MW)[30], which indicates that these nonlinear effects can be triggered during the exit surface damage process. Thus, laser energy used to support the exit surface LPP is further limited.

Figure 4 shows the typical emission spectra of plasmas on exit and input surfaces, respectively. It can be clearly

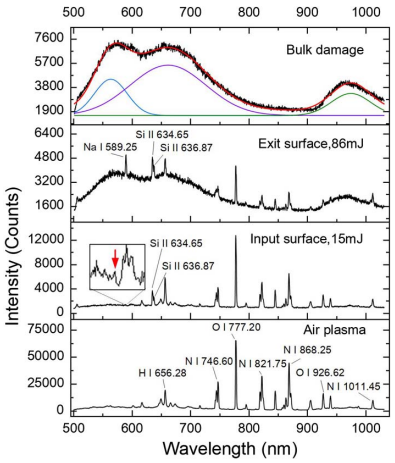

Fig. 4. Typical plasma emission spectra of bulk damage, exit surface damage, input surface damage, and air plasma from top to bottom. Lines superimposed on the bulk spectra are the fitted line and three Gaussian components. The wavelength range of the inset in the input surface spectra is 572–610 nm. The red arrow indicates the wavelength of 589.25 nm.

seen that multiple peaks are detected in the range of 500–1030 nm. Details of the main peaks, including their wavelengths and species are labelled near the peak. The emission lines on the exit surface plasma are much weaker than the input surface ones. This can be explained by the weaker coupling between the laser and plasma in exit surface damage, and thus, fewer atoms are ionized. As the emission intensity is proportional to the number density of particles, the exit surface plasma lines are therefore less intensive. For better understanding of the origin of spectra, the emission spectra of bulk damage plasma and air plasma are also shown in the first and last rows. The bulk damage spectra were collected by focusing the laser in the middle of the sample. In this case, no surface damage can be observed. As shown in Fig. 4, the spectra in input surface plasma exhibit like typical air plasma spectra except for those originated from Si II transitions. For the exit surface spectra, spectra from Si II, H I, O I, N I only appear at high energies (larger than 60 mJ), and only the Na I line at 589.25 nm can be observed at lower energies. This is because the Na I 589 nm doublet line has the lowest excitation energy (~1.61 eV) compared to other lines observed in this figure. The Na I peak (589.25 nm line) can also be observed in the input surface spectra but with a lower signal background ratio, as shown in the inset of the 15 mJ spectra. The line is also observed in other works focusing on laser ablation of glass[31], and the sodium is expected to be used as a dopant in the polishing process[32]. It is somewhat unexpected that emission lines of exit surface LPP are superimposed on a continuum background. As this background is analogous to the bulk damage spectra, it is reasonable to believe that this continuum is from the scattered bulk signal. Actually, it is widely observed that exit surface damage of fused silica is accompanied by a prominent damage in bulk material[23,25,33], which makes the above assumption more plausible. Origins of this continuum will be discussed later.

Stark broadening of the H_α line at 656 nm is used to estimate the electron number density in plasma. Choosing the H_α line is due to (i) well recognized line shape, (ii) negligible self-absorption at relatively low electron density ($<10^{-18}$ cm^{-3})[34], and (iii) well defined broadening parameters. Considering both the ion and electron broadening, the electron density N_e can be expressed as[34,35]

$$N_e(\mathrm{H}_\alpha) = 8.02 \times 10^{12}\left[\frac{\Delta\lambda_s}{\alpha_{1/2}(N_e, T)}\right]^{3/2} \mathrm{cm}^{-3}, \quad (3)$$

where $\Delta\lambda_s$ is the FWHM line width in angstrom, $\alpha_{1/2}(N_e, T)$ is the half-width of the reduced Stark profile in angstrom, and T is excitation temperature in K. $\alpha_{1/2}(N_e, T)$ is a weak function of N_e and T and can be found in Ref. [36]. The plasma excitation temperature T is retrieved using the standard Boltzmann plot method. Thus, the relation between line intensity I_{ji} (j and i indicate the upper and lower energy levels, respectively) and energy of j level E_j can be expressed as[34]

$$\ln\left(\frac{I_{ji}\lambda_{ji}}{A_{ji}g}\right) = -\frac{1}{kT}E_j + \ln\left[\frac{hcN}{4\pi U(T)}\right], \quad (4)$$

where λ_{ji} is the wavelength, A_{ji} and g are the Einstein coefficient and statistical weight of level j, $U(T)$ is the partition function, N is the number density of corresponding species, and h, c, k have the usual meaning. As a result, T can be deduced from the slope of this plot. Lines used to calculate the excitation temperature should be with enough large excitation energy and free from the self-absorption effect[37]. Three lines (777 nm, 844 nm, and 926 nm) from O I transitions fulfilling these requirements[37] are selected for temperature calculation, and their detailed spectroscopic data are shown in Table 1.

Evaluated electron density and excitation temperature of exit and input surface LPPs are shown in Fig. 5. As the necessary lines to deduce N_e and T of the exit surface LPP can only be observed at limited energies, the data quantity is much less than the input surface LPPs. The highest energy for input surface LPP only reaches 33.5 mJ to avoid saturation of the spectrometer. Similar to the plasma size, the electron density and temperature also increase with the laser energy on both surfaces. The maximum N_e and T for exit surface LPP are 3.2×10^{17} cm^{-3} and 0.69 eV, while the input surface LPP shows

Table 1. Spectroscopic Data Used for Temperature Calculation

Species	λ_{ji} (nm)	A_{ji} (10^7 s^{-1})	g	E_j (eV)
O I	777.383	3.69	15	10.74
	844.646	3.22	9	10.99
	926.315	2.47	45	12.08

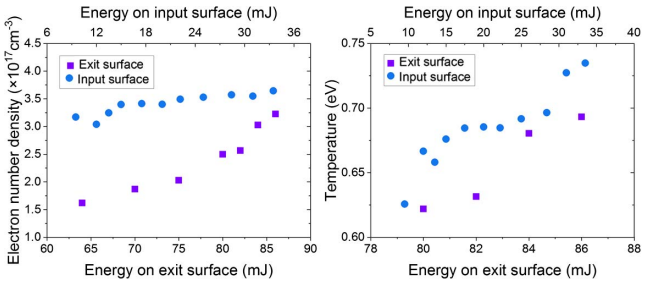

Fig. 5. Evaluated electron density and excitation temperature of exit and input surface LPPs.

significantly larger maximum values, although the energy there is much smaller. A larger number of ionized species and more frequent collision due to stronger laser–plasma coupling on the input surface LPP are attributed to the reason. Note that the Boltzmann plot method needs the local thermodynamic equilibrium (LTE) to be fulfilled. This can be examined by a necessary condition named the McWhirter criterion[34]:

$$N_e \geq 1.6 \times 10^{12} T^{0.5} \Delta E^3 \text{ cm}^{-3}, \quad (5)$$

where ΔE is the largest energy of considered transitions in eV, and T is in K. The maximum ΔE in this work is 1.59 eV for the 777.383 nm line, and the maximum temperature is 0.73 eV (8471 K). The minimum N_e for LTE is then calculated to be 5.9×10^{14} cm^{-3}, which is much smaller than the deduced values ($\sim 10^{17}$ cm^{-3}). Thus, the above criterion is satisfied.

It is worth noting that the origin of the continuum background of the exit surface LPP spectra is still unclear. Before discussing this, it is helpful to elucidate the damage mechanism in bulk silica. For bulk damage, it is more deterministic, as the impurity density is much lower than the surface, and the damage is mainly due to optical breakdown. Plasma produced in this case is strongly confined by surrounding bulk materials and, therefore, has a high electron number density. It is estimated that electron number density during bulk damage can reach 10^{19} cm^{-3} according to our previous time-resolved transmission measurement[38]. This is two magnitudes higher than the surface plasma shown in Fig. 5. The high-density effect is known to cause the deduction of ionization energy and the broadening of lines[39]. Therefore, it facilitates the formation of wide continuum radiation. Another explanation would be to attribute this continuum to the luminescence emitted by defects in bulk silica formed during the damage process. Solved using the Gaussian fitting procedure, the continuum contains three wide peaks at 563.37 nm (FWHM = 66 nm), 661.33 nm (FWHM = 152 nm), and 974.08 nm (FWHM = 79 nm). These Gaussian components and the overall fitted line are shown in the top of Fig. 4 as superimpositions on the bulk spectra. Actually, laser-induced formation of defects in SiO_2 has been widely reported from nanosecond to femtosecond laser irradiation[40,41]. Specifically, the 661.33 nm (1.9 eV) and 974.08 nm (1.3 eV) bands have been well recognized and are attributed to the nonbridging oxygen hole center (NBOHC) and Si nanocluster, respectively[42–44]. NBOHC is formed by the stress and shock-wave-induced plastic deformations and cracking of bulk silica[42]. The formation of a Si nanocluster is probably due to the thermal dissociation of oxygen and subsequent phase separation[44]. The 563.37 nm (2.2 eV) band, though often observed in other LID work[43], is not well defined and is attributed to the strain relaxation process in SiO_2 according to a recent work[45]. Identifying the origins of observed peaks needs quantitative evaluation such as the time-resolved lifetime measurement, which, however, is beyond the scope of current study and will be investigated in our future work.

In conclusion, optical emission properties, including spontaneous emission images and spectra during LID events, have been investigated. Larger plasma size, electron density, and temperature have been observed for the input surface LPP. Asymmetry in laser–plasma coupling on input and exit surfaces is employed to explain the phenomenon. Moreover, the exit surface LPP spectra are found to include a continuum background containing three peaks. Luminescence of defects formed during LID process is used to give a preliminary explanation.

This work was supported by the National Natural Science Foundation of China (No. 21735005).

References

1. D. Chu, K. Yin, X. Dong, Z. Luo, Y. Song, and J.-A. Duan, Chin. Opt. Lett. **16**, 011401 (2018).
2. T. He, C. Wei, Z. Jiang, Z. Yu, Z. Cao, and J. Shao, Chin. Opt. Lett. **16**, 041401 (2018).
3. S. Papernov and A. W. Schmid, J. Appl. Phys. **104**, 63101 (2008).
4. G. H. Hu, Y. A. Zhao, S. T. Sun, D. W. Li, X. F. Liu, X. Sun, J. D. Shao, and Z. X. Fan, Chin. Phys. Lett. **26**, 97802 (2009).
5. Z. Cao, H. He, G. Hu, Y. Zhao, L. Yang, and J. Shao, Chin. Opt. Lett. **17**, 051601 (2019).
6. Q. Zhou, R. Qiu, Y. Jiang, X. Gao, Y. Yang, H. Wang, and H. Ren, Chin. Opt. Lett. **14**, 051402 (2016).
7. K. R. P. Kafka and S. G. Demos, Opt. Lett. **44**, 1844 (2019).
8. X. Liu, Y. A. Zhao, D. Li, G. Hu, Y. Gao, Z. Fan, and J. Shao, Appl. Opt. **50**, 4226 (2011).
9. W. Sun, H. Qi, Z. Fang, Z. Yu, Y. Liu, K. Yi, and J. Shao, Opt. Express **22**, 2948 (2014).
10. A. Heins and C. Guo, J. Appl. Phys. **113**, 223506 (2013).
11. N. L. Boling, G. Dubé, and M. D. Crisp, Appl. Phys. Lett. **21**, 487 (1972).
12. A. Salleo, F. Y. Génin, M. D. Feit, A. M. Rubenchik, T. Sands, S. S. Mao, and R. E. Russo, Appl. Phys. Lett. **78**, 2840 (2001).
13. H. Liu, X. Zhou, J. Huang, F. Wang, X. Jiang, J. Huang, W. Wu, and W. Zheng, Acta Phys. Sin. **60**, 065202 (2011).
14. X. Zeng, S. S. Mao, C. Liu, X. Mao, R. Greif, and R. E. Russo, Spectrochim. Acta Part B: Atom. Spectrosc. **58**, 867 (2003).
15. X. Zeng, S. S. Mao, C. Liu, X. Mao, R. Greif, and R. E. Russo, Appl. Phys. Lett. **83**, 240 (2003).
16. X. Zeng, X. Mao, S. S. Mao, J. H. Yoo, R. Greif, and R. E. Russo, J. Appl. Phys. **95**, 816 (2004).
17. X. Zeng, X. Mao, S. S. Mao, S. B. Wen, R. Greif, and R. E. Russo, Appl. Phys. Lett. **88**, 061502 (2006).

18. R. N. Raman, S. Elhadj, R. A. Negres, M. J. Matthews, M. D. Feit, and S. G. Demos, Opt. Express **20**, 27708 (2012).
19. C. D. Harris, N. Shen, A. M. Rubenchik, S. G. Demos, and M. J. Matthews, Opt. Lett. **40**, 5212 (2015).
20. S. S. Harilal, P. K. Diwakar, M. P. Polek, and M. C. Phillips, Opt. Express **23**, 15608 (2015).
21. V. Lazic, J. J. Laserna, and S. Jovicevic, Spectrochim. Acta Part B: Atom. Spectrosc. **82**, 42 (2013).
22. P. Serra, J. Palau, M. Varela, J. Esteve, and J. L. Morenza, J. Mater. Res. **10**, 473 (1995).
23. S. G. Demos, R. A. Negres, R. N. Raman, A. M. Rubenchik, and M. D. Feit, Laser Photon. Rev. **7**, 444 (2013).
24. J. Wong, J. L. Ferriera, E. F. Lindsey, D. L. Haupt, I. D. Hutcheon, and J. H. Kinney, J. Non-Cryst. Solids **352**, 255 (2006).
25. C. W. Carr, J. D. Bude, and P. DeMange, Phys. Rev. B **82**, 184304 (2010).
26. S. G. Demos, R. A. Negres, R. N. Raman, M. D. Feit, K. R. Manes, and A. M. Rubenchik, Optica **2**, 765 (2015).
27. L. Zhaoxiang, W. Jinquan, S. Fenglou, and G. Shunsheng, Appl. Opt. **49**, C80 (2010).
28. X. Zeng, X. Mao, S. Wen, R. Greif, and R. E. Russo, J. Phys. D: Appl. Phys. **37**, 1132 (2004).
29. X. Zeng, X. L. Mao, R. Greif, and R. E. Russo, Appl. Phys. A **80**, 237 (2005).
30. A. V. Smith and B. T. Do, Appl. Opt. **47**, 4812 (2008).
31. C. Gerhard, J. Hermann, L. Mercadier, L. Loewenthal, E. Axente, C. R. Luculescu, T. Sarnet, M. Sentis, and W. Viöl, Spectrochim. Acta Part B: Atom. Spectrosc. **101**, 32 (2014).
32. J. Bude, P. Miller, S. Baxamusa, N. Shen, T. Laurence, W. Steele, T. Suratwala, L. Wong, W. Carr, D. Cross, and M. Monticelli, Opt. Express **22**, 5839 (2014).
33. A. M. Rubenchik, M. D. Feit, and S. G. Demos, Proc SPIE **8885**, 88851D (2013).
34. W. Lei, V. Motto-Ros, M. Boueri, Q. Ma, D. Zhang, L. Zheng, H. Zeng, and J. Yu, Spectrochim. Acta Part B: Atom. Spectrosc. **64**, 891 (2009).
35. A. M. El Sherbini, H. Hegazy, and T. M. El Sherbini, Spectrochim. Acta Part B: Atom. Spectrosc. **61**, 532 (2006).
36. P. Kepple and H. R. Griem, Phys. Rev. **173**, 317 (1968).
37. H. Hegazy, Appl. Phys. B **98**, 601 (2010).
38. C. Shen, M. Chambonneau, X.-A. Cheng, Z. Xu, and T. Jiang, Appl. Phys. Lett. **107**, 111101 (2015).
39. H. R. Griem, *Principles of Plasma Spectroscopy* (Cambridge, 1997).
40. S. G. Demos, M. Staggs, K. Minoshima, and J. Fujimoto, Opt. Express **10**, 1444 (2002).
41. A. Zoubir, C. Rivero, R. Grodsky, K. Richardson, M. Richardson, T. Cardinal, and M. Couzi, Phys. Rev. B **73**, 224117 (2006).
42. S. O. Kucheyev and S. G. Demos, Appl. Phys. Lett. **82**, 3230 (2003).
43. J. Fournier, J. Néauport, P. Grua, E. Fargin, V. Jubera, D. Talaga, and S. Jouannigot, Opt. Express **18**, 21557 (2010).
44. R. Salh, L. Fitting, E. V. Kolesnikova, A. A. Sitnikova, M. V. Zamoryanskaya, B. Schmidt, and H. J. Fitting, Semiconductors **41**, 381 (2007).
45. J. Zhou and B. Li, Opt. Mater. Express **7**, 2888 (2017).